CrossMark

ORIGINAL PAPER

Energy-Based Analysis of Mechanisms of Earthquake-Induced Landslide Using Hilbert–Huang Transform and Marginal Spectrum

Gang Fan[1] · Li-Min Zhang[1] · Jian-Jing Zhang[2] · Fang Ouyang[2]

Abstract Based on the Hilbert–Huang Transform and its marginal spectrum, an energy-based method is proposed to analyse the dynamics of earthquake-induced landslides and a case study is presented to illustrate the proposed method. The results show that the seismic Hilbert energy in the sliding mass of a landslide is larger than that in the sliding bed when subjected to seismic excitations, causing different dynamic responses between the sliding mass and the sliding bed. The seismic Hilbert energy transits from the high-frequency components to the low-frequency components when the seismic waves propagate through the weak zone, causing a nonuniform seismic Hilbert energy distribution in the frequency domain. Shear failure develops first at the crest and toe of the sliding mass due to resonance effects. Meanwhile, the seismic Hilbert energy in the frequency components of 3–5 Hz, which is close to the natural frequency of the slope, is largely dissipated in the initiation and failure processes of the landslide. With the development of dynamic failure, the peak energy transmission ratios in the weak zone decrease gradually. This study offers an energy-based interpretation for the initiation and progression of earthquake-induced landslides with the shattering-sliding failure type.

1 Introduction

Earthquake-induced landslides are one of the most destructive natural hazards and led to enormous loss of property and human lives. The 12 May 2008 Wenchuan earthquake (M_L 7.9) in Western China triggered more than 56,000 landslides in steep mountainous terrains coving an area of about 41,750 km^2 (Dai et al. 2011). These landslides directly caused more than 20,000 fatalities (Yin et al. 2009). In recent years, many researchers paid their attention to the earthquake-induced landslide spatial distribution (Bjerrum et al. 2010; Dai et al. 2011; Huang and Li 2009; Zhang et al. 2014), earthquake-induced landslide susceptibility (Ding and Hu 2014; Chang et al. 2005), dynamic failure mechanisms (Guo and Hamada 2013; Huang et al. 2012; Li et al. 2012; Zhou et al. 2013), etc. Many techniques have been utilized to analyse the dynamic stability and failure mechanisms of slopes, including the fuzzy-based method (Champati et al. 2007), the viscoplastic behaviour model (Grelle et al. 2011; Grelle and Guadagno 2013), the cumulative displacement method (Peng et al. 2009) and other types of numerical methods (Tang et al. 2009; Wu et al. 2009; Zhou et al. 2013; Li et al. 2012). These techniques are helpful for understanding the initiation and dynamic failure mechanisms of earthquake-induced landslides.

✉ Li-Min Zhang
cezhangl@ust.hk

Gang Fan
fangang@ust.hk

Jian-Jing Zhang
jianzhang1102@home.swjtu.edu.cn

Fang Ouyang
ouyangfang26@126.com

[1] Department of Civil and Environmental Engineering, The Hong Kong University of Science and Technology, Clear Water Bay, Hong Kong, People's Republic of China

[2] Department of Geotechnical Engineering, Southwest Jiaotong University, Chengdu, Sichuan, People's Republic of China

Seismic energy is a fundamental trigger of landslide initiation and dynamic failure. Therefore, it is extremely important to reveal the initiation and dynamic mechanisms of landslides from the viewpoint of seismic energy. In recent decades, energy-based methods have drawn attention in geotechnical engineering, including elastoplastic damage theories and failure criterion of rock (Hao and Liang 2016; Ju 1989), rock burst intensity classification (Chen et al. 2015), rock brittleness index and quantification (Munoz et al. 2016), and energy dissipation and release during rock failure (Meng et al. 2016; Peng et al. 2015; Tang and Kaiser 1998; Zhang et al. 2000). However, the existing studies mainly focused on the static energy in the rock mass, little attention has been paid to the seismic energy and energy-based interpretation of the initiation and failure of earthquake-induced landslides.

Since it was put forward by Huang et al. (1998), the Hilbert–Huang Transform (HHT) and its marginal spectrum have been widely adopted in many areas of geophysics, including seismic, climatic, atmospheric, groundwater and sea waves (Crockett and Gillmore 2010; Dong et al. 2008, 2010; Fan et al. 2016a, b; Feng 2011; Poon and Chang 2007; Rehman and Mandic 2010; Yu et al. 2010; Zhang et al. 2016). However, the HHT has not been fully utilized in geotechnical engineering. The existing studies indicate that this new decomposition technique is adaptive and highly efficient. Most importantly the HHT is suitable for processing nonstationary and nonlinear signals, e.g. earthquake waves. Based on the HHT, the marginal spectrum of the original signal can be obtained, which denotes the seismic Hilbert energy distribution of the signal in the frequency domain.

In the present study, based on the HHT signal processing technique and its marginal spectrum, large-scale shaking table tests and numerical simulations, an attempt is made to demonstrate the energy-based method in interpreting the dynamic mechanisms of earthquake-induced landslides with the shattering-sliding failure type.

2 Methodology

2.1 Concepts of HHT and Marginal Spectrum

Huang et al. (1998) proposed a signal processing method for analysing nonlinear and nonstationary data, namely Hilbert–Huang Transform (HHT), which has been widely used in several applications. A key part of HHT is empirical mode decomposition (EMD), with which any complicated data set can be decomposed into a finite and often small number of intrinsic mode functions (IMF) that admit well-behaved Hilbert transform. The EMD method is a necessary pre-processing of the data before the Hilbert

transform can be applied. Based on the Hilbert transform, the Hilbert spectrum of the original signal can be calculated, and finally the marginal spectrum of the original signal can be obtained. The Hilbert spectrum presents simultaneously the wave amplitude, instantaneous frequency and time of the original wave in a three-dimensional plot. In wave dynamics, the squared amplitude is frequently used to represent the energy density of the original wave; hence, the Hilbert spectrum represents the seismic Hilbert energy of the original wave. The marginal spectrum offers a measure of total Hilbert energy contribution from each frequency value and corresponds to a Hilbert energy density at frequency ω. The marginal spectrum represents the cumulated Hilbert energy of the original signal over the entire data span in a probabilistic sense. A brief introduction to the HHT signal processing method and an HHT example on the El Centro earthquake wave are presented in "Appendix".

The Hilbert transform has obvious advantages in processing the nonstationary and nonlinear signals over traditional signal processing technologies, i.e. Fourier transform and Wavelet transform. In the Hilbert transform, the frequencies of the waves are modelled by sub-harmonics, which serve as an indicator of nonlinearity, while the frequencies of the waves are modelled as superimposed constant frequency and sinusoidal components in the Fourier transform. These Fourier components are a mathematically correct decomposition for the data, but they do not make physical sense and are not suitable for nonstationary and nonlinear signals such as earthquake waves, since pure sinusoidal waves are not a solution for any equation governing earthquake waves. The wavelet spectrum, while correctly depicting the front–back asymmetry, has been shown to give poor frequency resolution, especially in the low-frequency domain. Detailed comparisons between the Fourier transform, the Wavelet transform and the Hilbert transform for processing water waves and weekly mortgage rate data were presented by Huang et al. (1999, 2003). Both the Fourier and Wavelet representations are shown to be inferior to the Hilbert result.

2.2 Energy-Based Analysis Method

The seismic Hilbert energy, which can be quantitatively presented by the marginal spectra, is a trigger of earthquake-induced landslides. Since a slope is characterized with dynamic features, the distribution of seismic Hilbert energy in the frequency domain is significant for revealing the dynamic mechanisms of earthquake-induced landslides. Based on the concepts of the HHT and its marginal spectrum, the seismic Hilbert energy distribution in the frequency domain can be identified.
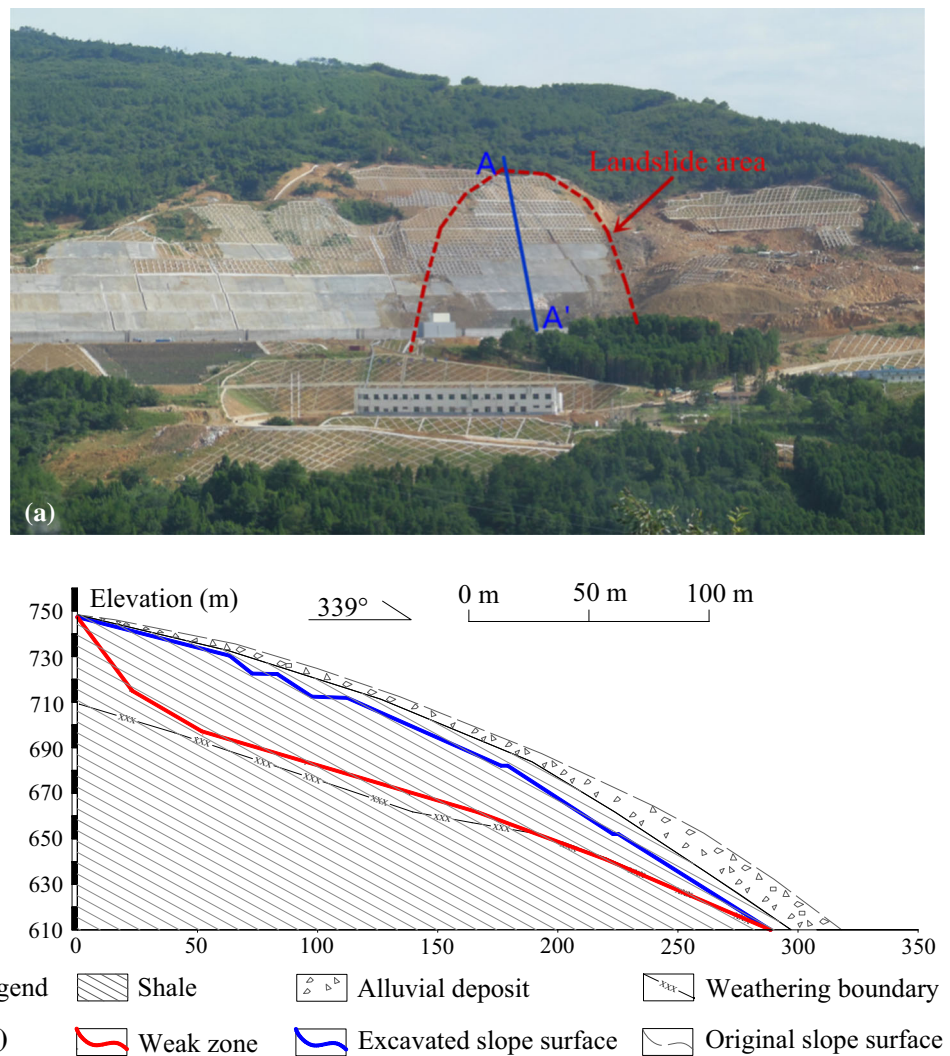
When the seismic wave propagates through the slope with a weak zone, the seismic wave amplitude and the seismic Hilbert energy distribution in the frequency domain will change significantly. On the one hand, the seismic Hilbert energy amplitude at different parts of the slope will be different due to complex reflections on the slope surface and refraction in the weak zone. On the other hand, the seismic Hilbert energy distribution in the frequency domain will be influenced by the weak zone. Since the slope mass itself is characterized with dynamic features in the frequency domain, changes in the distribution of seismic Hilbert energy in the frequency domain will affect the dynamic response of the slope, which may trigger the failure of the slope. By analysing changes in the seismic Hilbert energy amplitude and distribution in the frequency domain, combining with the observed phenomena in the initiation and failure processes of the earthquake-induced landslide, the initiation and failure mechanism can be revealed and interpreted from the viewpoint of seismic Hilbert energy. For this reason, the proposed analysis method in this study can be defined as an energy-based method.

The dynamic failure mechanism of the earthquake-induced landslide is analysed by the energy-based method proposed in this study in the following steps:

1. Carry out EMD after measuring the acceleration time histories at different locations in the model slope and obtain a series of IMF components;
2. Conduct the Hilbert transform on each IMF to obtain first the instantaneous frequency and then the Hilbert marginal spectrum of the original data;
3. Calculate the marginal spectra of all the acceleration measuring points in the model slope;
4. Identify the changes of seismic Hilbert energy distribution in the dynamic failure process of the model slope according to the varying rule of the marginal spectrum amplitude at all acceleration measuring points;
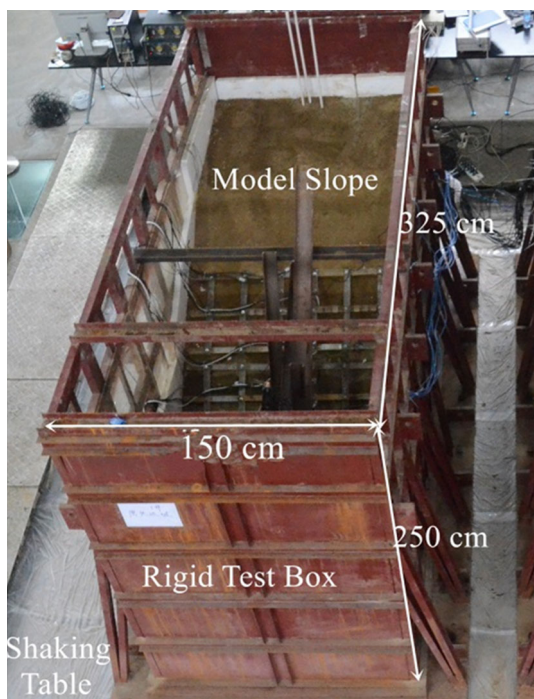5. Based on the identified change of seismic Hilbert energy distribution inside the model slope, the

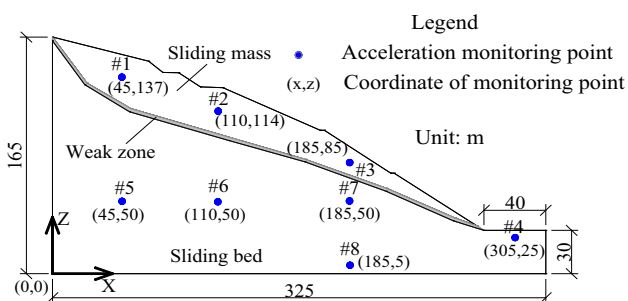Fig. 2 Model slope and rigid box for the shaking table test

Fig. 3 Full dimensions of the model slope and layout of the acceleration monitoring points

observations in the shaking table tests and numerical simulations, the initiation and failure mechanisms of the earthquake-induced landslides can be determined from the viewpoint of seismic Hilbert energy.

3 Application of Energy-Based Method to an Earthquake-Induced Landslide

3.1 Geological Conditions of the Landslide

The landslide under study is located in the mountainous area in Guangyuan City, Sichuan Province, China. It was formed due to excavation and earthquake events, as shown in Fig. 1a. In the rainy seasons after the 12 May 2008 Wenchuan earthquake, the excavated slope started to move

Table 1 Similarity scaling factors for the shaking table test

Parameter	Similarity ratio
Physical dimension (L)	$C_L = 100$
Density (ρ)	$C_\rho = 1$
Acceleration (a)	$C_a = 1$
Elasticity modulus (E)	$C_E = 100$
Stress (σ)	$C_\sigma = 100$
Strain (ε)	$C_\varepsilon = 1$
Force (F)	$C_F = 1{,}000{,}000$
Velocity (V)	$C_V = 10$
Time (t)	$C_t = 10$
Displacement (u)	$C_u = 100$
Angular displacement (θ)	$C_\theta = 1$
Frequency (ω)	$C_\omega = 0.1$
Damping ratio (ζ)	$C_\zeta = 1$
Internal friction angle (φ)	$C_\varphi = 1$

at a rate of 1–2 mm/day, and some tensile cracks were observed on the trailing edge of the landslide. The height of the slope is 135 m, the slope angle is 38°, and the volume of the landslide is about 478,000 m³. The sliding bed is mainly formed in intact shale. The sliding mass consists of weathered shale and alluvial deposit, among which the alluvial deposit was excavated; hence, the sliding mass only consists of weathered shale. The weak zone consists of silty clay. The longitudinal profile of the landslide is illustrated in Fig. 1b.

In the past decade, two strong earthquakes struck this area, including the 12 May 2008 Wenchuan earthquake and the 20 April 2013 Lushan earthquake. The distance between the landslide and the earthquake-triggering fault zone (Longmenshan) is approximately 260 km. Considering the importance of the site and constructions near the landslide, it is essential to reveal the dynamic mechanism of this landslide for hazard mitigation.

3.2 Shaking Table Test

The materials in the test model were mainly sand, clay, plaster, water and barite at ratios of 1:0.6:0.5:0.28:0.8 for the sliding bed and 1:0.4:0.1:0.3:0.2 for the sliding mass. The materials in the test model were mixed according to the mix proportion obtained in previous laboratory experiments. The materials in the weak zone were obtained from the prototype landslide and remodelled for the test model. The maximum thickness of the weak zone in the prototype slope was 30 cm; therefore, the thickness of the weak zone was 0.3 cm in the model according to the similarity ratio for physical dimension. The bottom surface size of the test model was 325 × 150 cm, and the height of the test model was 165 cm. The length of the model slope was 325 cm,

Table 2 Material parameters

Material	Bulk modulus E (GPa)	Shear modulus G (MPa)	Density (g/cm³)	Poisson's ratio	Cohesion (MPa)	Internal friction angle (°)
Sliding mass	1.67	0.77	2.1	0.3	8	40
Weak zone	0.0256	0.0073	1.95	0.37	0.015	22
Sliding bed	6.67	4.0	2.4	0.25	20	60

Fig. 4 Input horizontal and vertical El Centro seismic waves with a peak amplitude of 0.1 g: **a** horizontal time history, **b** vertical time history, **c** Fourier spectrum of horizontal time history and **d** Fourier spectrum of vertical time history
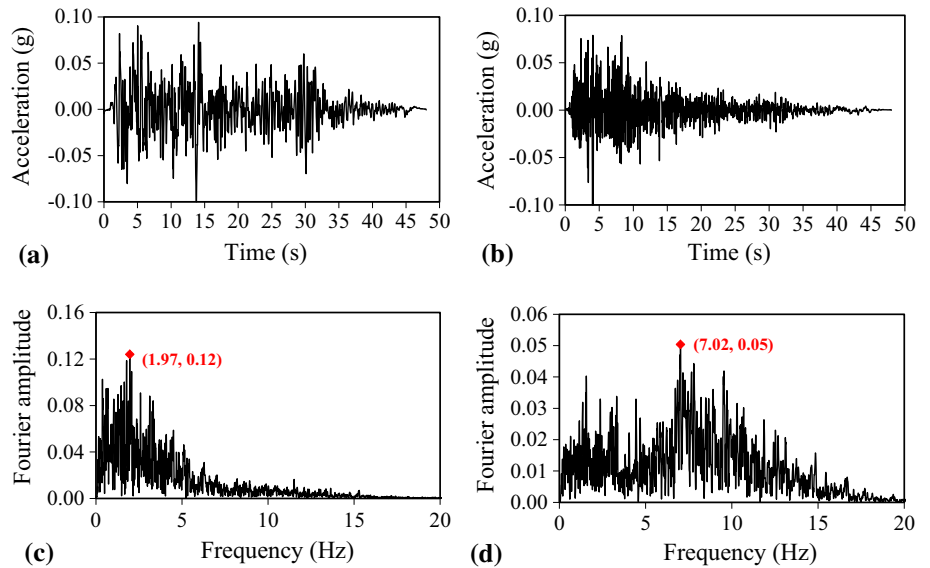
Table 3 Test loading sequence

No.	Waveform	Amplitude (g)
1	White noise	0.1
2	El Centro	0.1
3	White noise	0.1
4	El Centro	0.3
5	White noise	0.1
6	El Centro	0.5
7	White noise	0.1
8	El Centro	0.7
9	White noise	0.1
10	El Centro	0.9

Fig. 5 Transfer functions based on white noise waveform excitation at the first stage of shaking table test

which, according to existing studies (Liu et al. 2013, 2014), is an acceptable value for physical model test using a shaking table. The test model and rigid test box are shown in Fig. 2. In the test, a 5-cm thick absorber made of foam materials was placed on the four sides of the rigid test box to minimize the influence of the container boundaries on the input seismic waves. Although the absorber might influence the displacements of the test model, Whitman and Lambe (1986) and Liu et al. (2013, 2014) indicated that this approach allows for a "reasonably correct"
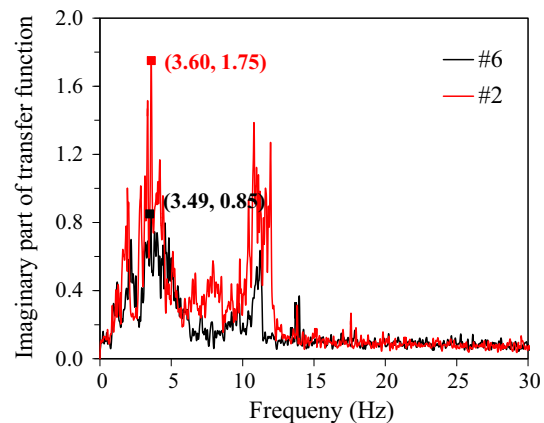
boundary. The geometric sizes and the layout of the acceleration monitoring points for the shaking table test are shown in Fig. 3.

In reference to Buckingham's π theorem of similarity, the dimension L, mass density ρ and acceleration a were chosen as the fundamental parameters with scaling factors of $C_L = 100$, $C_\rho = 1$ and $C_a = 1$, respectively. The similarity scale factors for the physical parameters in this shaking table test are listed in Table 1.

Fig. 6 2D Hilbert energy distributions at acceleration monitoring points #1–#8 in the time–frequency domain under the excitation of 0.3 g El Centro earthquake wave: **a** #1, **b** #2, **c** #3, **d** #4, **e** #5, **f** #6, **g** #7 and **h** #8. The chromatic change denotes the values of seismic Hilbert energy
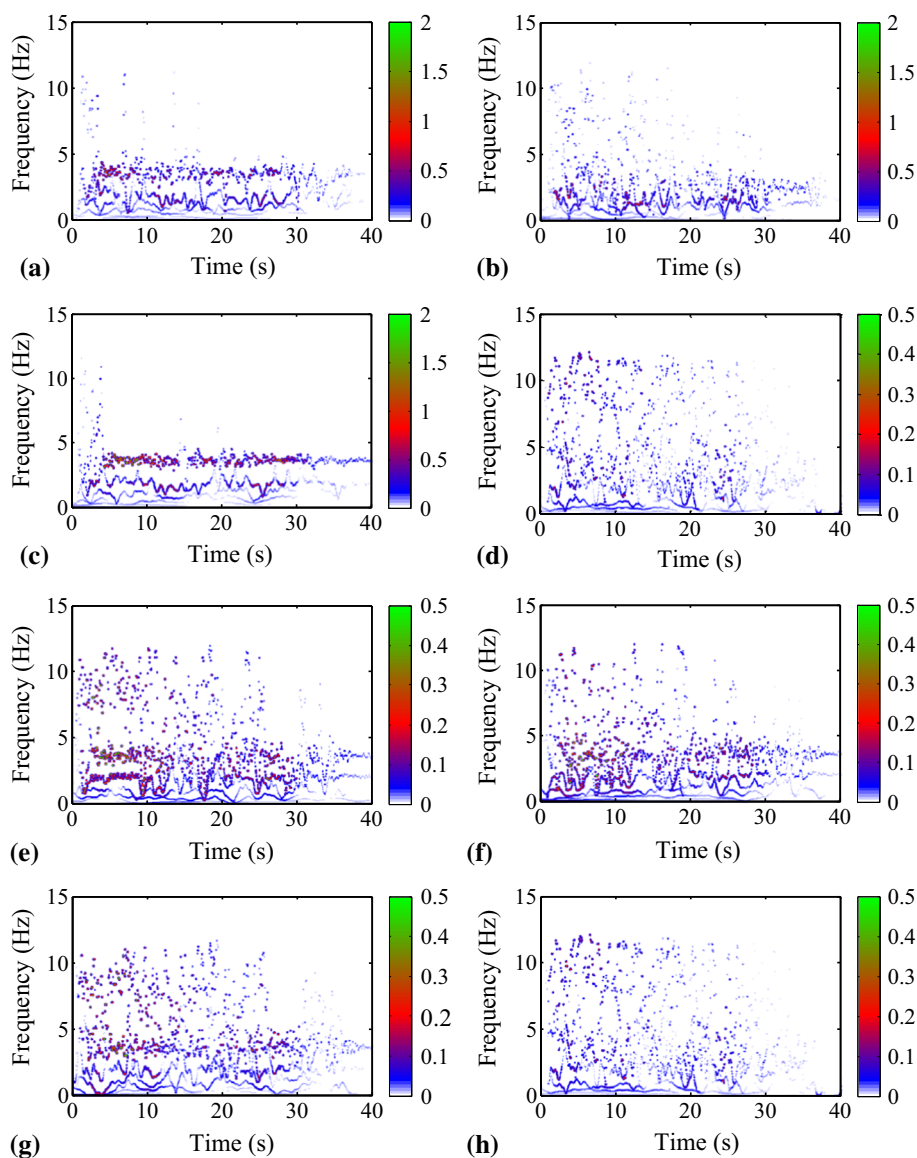
After the model test was completed, samples were taken from the test model to obtain physical parameters in the laboratory. The physical parameters of the test model are shown in Table 2.
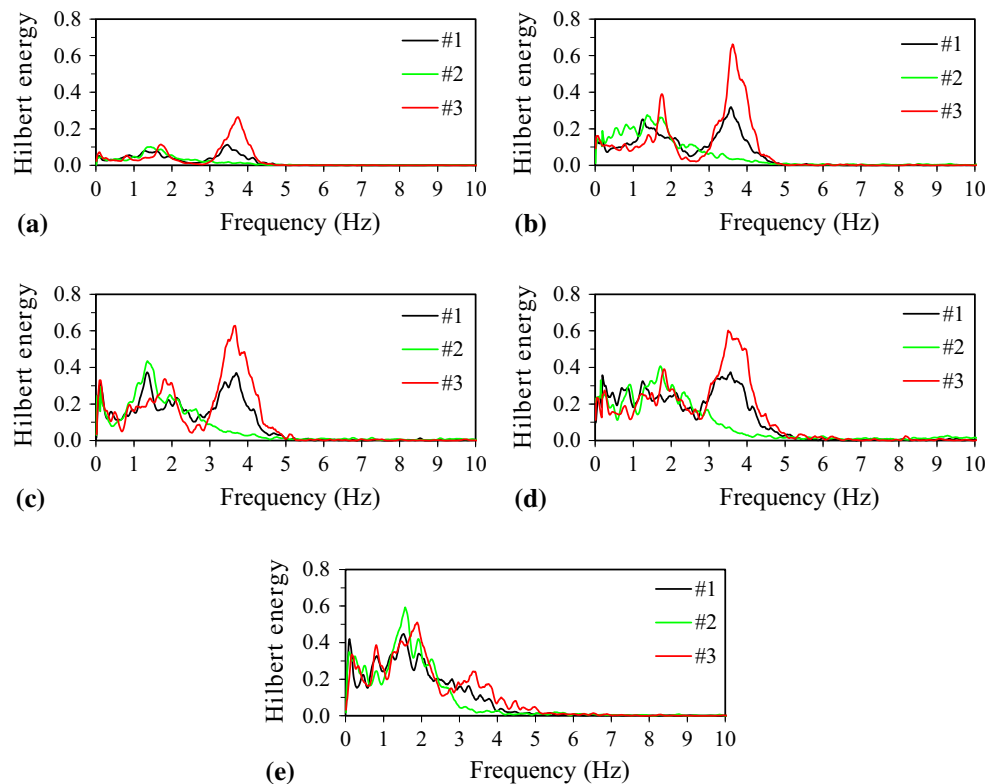
The loading waveform used in this shaking table test was an El Centro earthquake record, selected because it has been widely used in earthquake engineering around the world. According to the similarity criteria, the input earthquake records were compressed in the time axis at a compression ratio of 10 (the time similarity ratio). The acceleration time histories and Fourier spectra of horizontal and vertical El Centro earthquake records with an amplitude of 0.1 g are shown in Fig. 4.

Two simultaneous loading directions of experimental earthquake excitation were applied, namely the horizontal or X direction, and the vertical or Z direction. In this shaking table test, the horizontal peak accelerations of

loading waveforms were scaled to 0.1, 0.3, 0.5, 0.7 and 0.9 g. A large number of field investigations show that the vertical peak acceleration is usually two-thirds of the horizontal peak acceleration (Ambraseys and Douglas 2003; Bozorgnia et al. 1995; Theodulidis and Bard 1995); hence, the vertical peak accelerations of loading waveform were scaled to be 0.067, 0.201, 0.335, 0.469 and 0.603 g correspondingly. The model was subject to 0.1 g white noise scanning before the excitation of each input earthquake record. The loading sequence of the shaking table test is shown in Table 3.

The test started by exciting the test model with a white noise wave with a flat Fourier spectrum in all frequencies to obtain the initial dynamic characteristics of the test model. Based on the responding signals of the test model under white noise excitation, transfer functions of the test model were obtained. Our previous studies show that the

Fig. 7 Marginal spectra for the acceleration monitoring points in the sliding mass (#1, #2 and #3) under the El Centro earthquake waves with different amplitudes: **a** 0.1 g; **b** 0.3 g; **c** 0.5 g; **d** 0.7 g and **e** 0.9 g

3.3 Analysis of Seismic Hilbert Energy Distribution

The Hilbert–Huang Transform (HHT) offers a viable tool to identify the seismic Hilbert energy distribution in the time–frequency domain. The Hilbert spectra of all acceleration monitoring points, i.e. #1–#8, under the 0.3 g El Centro earthquake wave are shown in Fig. 6. It can be seen that the seismic Hilbert energy distributes dispersedly in the time axis, but mainly in the range of 0–30 s. Acceleration monitoring points #1, #2 and #3 are all located in the sliding mass, the seismic Hilbert energy distributes mainly in the frequency range of 0–5 Hz, while the seismic Hilbert energy at acceleration monitoring points #4–#8, both of which are located in the sliding bed, distributes mainly in the frequency range of 0–12 Hz. It also can be seen that the peak seismic Hilbert energy amplitudes at #1, #2 and #3 acceleration monitoring points are larger than those at #4–#8.

According to the definition of marginal spectrum, the marginal spectrum of each acceleration monitoring point can be obtained. Taking the acceleration monitoring points in the sliding mass as examples, i.e. #1, #2 and #3, the marginal spectra of which under the excitations with different amplitudes are calculated and shown in Fig. 7. The marginal spectrum curves for #1 and #3 have two peaks, the first of which appearing in the frequency range of 1–2 Hz and the second in the frequency range of 3–5 Hz. While the marginal spectrum curve for #2 has only one peak appearing in the frequency range of 1–2 Hz, which coincides with the appearing frequency range of the first peaks of #1 and #3, and no obvious peaks are observed in the frequency range of 3–5 Hz. The peaks of #1, #2, and #3 in the frequency range of 1–2 Hz are close and increase gradually with increasing input amplitude. In the frequency range of 3–5 Hz, when the input amplitude reaches 0.3 g, the peaks of the marginal spectrum of #3 start to decrease and suffer a drastic decrease when the input amplitude reaches 0.9 g. Before the input amplitude reaches 0.7 g, the peak of marginal spectrum of #1 increases gradually with increasing input amplitude, but the increasing ratio becomes smaller and smaller, particularly when the input amplitude reaches 0.9 g. The peaks of the marginal
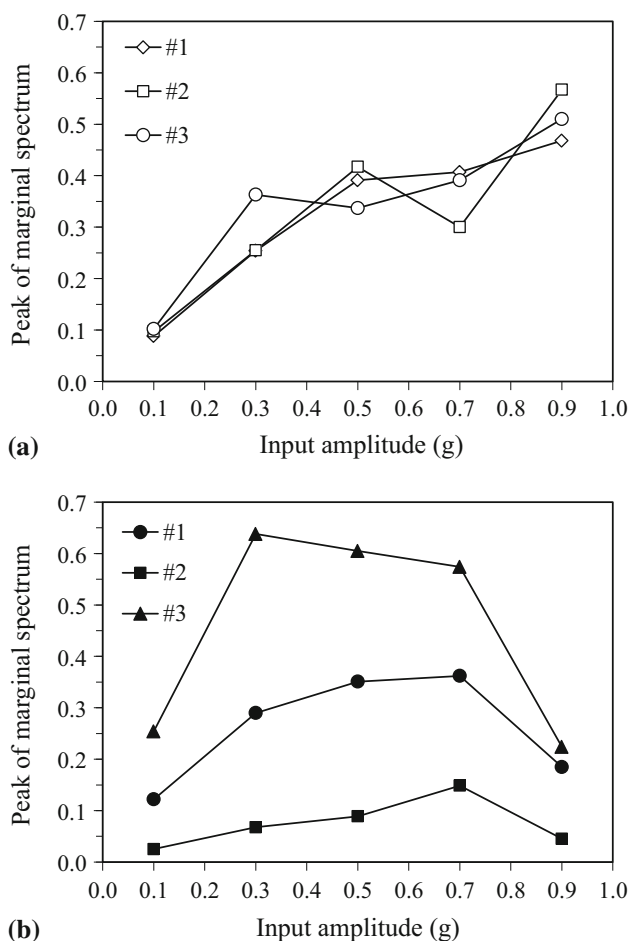
The dominant frequency of the imaginary part of the transfer function is more stable for calculating the natural frequency of the test model than those of the real part and the modulus of the transfer function (Fan et al. 2016a, b, 2017). Hence, the imaginary parts of the transfer functions of monitoring points #6 and #2 are utilized in this study to estimate the natural frequency of the model slope. The transfer functions for the X direction excitation calculated from the monitoring data at points #6 and #2 are shown in Fig. 5. The average dominant frequency is regarded as the natural frequency of the test model at the first stage of the test. In Fig. 5, the natural frequency of the test model for the X direction excitation is 3.55 Hz.

(a)

(b)

Fig. 8 Variation of peaks of marginal spectra with the input amplitude in the frequency ranges of 1–2 and 3–5 Hz
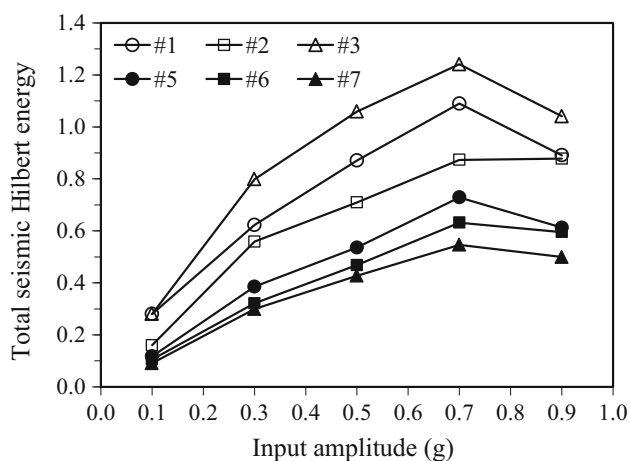

Fig. 9 Total seismic Hilbert energy at the acceleration monitoring points in the sliding mass (#1, #2 and #3) and the monitoring points in the sliding bed (#5, #6 and #7)

spectrum of #3 are larger than those of #1 in the frequency range of 3–5 Hz, especially when subjected to 0.3, 0.5 and 0.7 g seismic excitations, as shown in Fig. 8. For

comparison, the maximum values of the marginal spectrum of #2 in the frequency range of 3–5 Hz are regarded as the peaks of #2 and also plotted in Fig. 8b. The peaks of the marginal spectrum of #2 are much smaller than those of #1 and #3.

As the marginal spectrum offers a measure of total seismic Hilbert energy contribution from each frequency value, the area below the marginal spectrum curves in Fig. 7 represents the total seismic Hilbert energy over the entire frequency span. The total amounts of seismic Hilbert energy of the monitoring points in the sliding mass, i.e. #1, #2 and #3, are calculated and shown in Fig. 9. The total seismic Hilbert energy of acceleration monitoring points #5, #6 and #7, which are located in the sliding bed, is also calculated and shown in Fig. 9 for comparison. In the sliding mass, the total seismic Hilbert energy of #3 is the largest, followed by #1. The total seismic Hilbert energy of #2 is the smallest, which can be explained by that the seismic wave at acceleration monitoring point #2 does not carry much seismic Hilbert energy in the frequency range of 3–5 Hz, as shown in Fig. 7. At the same time, the total seismic Hilbert energy of the sliding mass is larger than that of the sliding bed. With the continuous excitation, the incident wave and the reflected wave may be superimposed when the incident wave reaches the slope surface, causing the seismic Hilbert energy stored in the sliding mass to be larger than that in the sliding bed.

The seismic Hilbert energy in the sliding mass comes from the energy transmitted through the weak zone; therefore, the study on the Hilbert energy transmission ratio of the weak zone is essential for revealing and interpreting the mechanism of the earthquake-induced landslides. In this study, the Hilbert energy transmission ratio is defined as the ratio of the marginal spectra in the sliding mass, i.e. acceleration monitoring points #1, #2 and #3, to the marginal spectra in the sliding bed, i.e. acceleration monitoring points #5, #6 and #7. If the Hilbert energy transmission ratio is larger than 1, it denotes an amplification effect; otherwise it denotes an attenuation effect. The Hilbert energy transmission ratios of the weak zone under different seismic wave excitations are calculated and shown in Fig. 10. To certify the influence of the weak zone on the seismic Hilbert energy distribution in the frequency domain, the Hilbert energy transmission ratios between acceleration monitoring points #7 and #8, both of which are located in the sliding bed, are also calculated and shown in Fig. 10.

The Hilbert energy transmission ratio between acceleration monitoring points #7 and #8 implies that the seismic Hilbert energy in the frequency range of 3–9 Hz is amplified observably when the seismic wave propagates in the sliding bed, especially in the frequency range of 7–9 Hz. In the crest and toe of the sliding mass, the seismic

Fig. 10 Transmission ratios of the marginal spectra under the El Centro seismic wave with different amplitudes: **a** 0.1 g; **b** 0.3 g; **c** 0.5 g; **d** 0.7 g and **e** 0.9 g
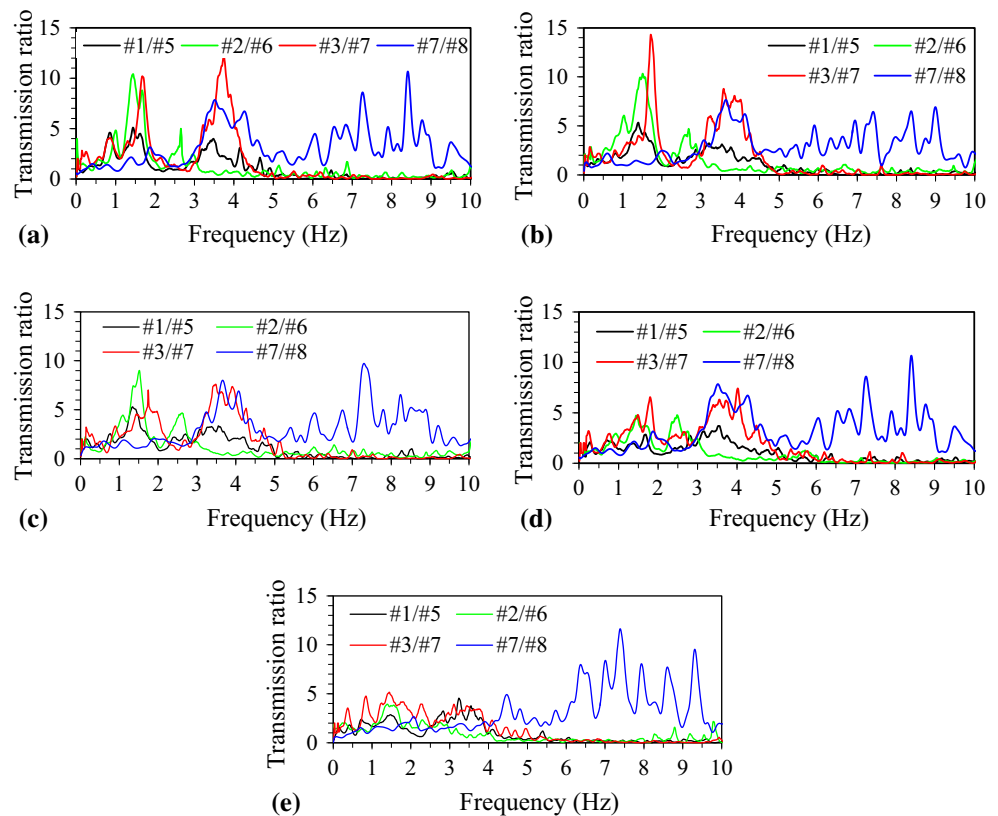
Hilbert energy in the frequency ranges of 1–2 and 3–5 Hz is amplified, while in the middle part of the sliding mass only the seismic Hilbert energy in the frequency range of 1–2 Hz is amplified. The seismic Hilbert energy in the frequency range larger than 5 Hz is attenuated by the weak zone significantly. That is to say when the seismic wave propagates through the weak zone, the seismic Hilbert energy in the high-frequency components is attenuated and the seismic Hilbert energy in the low-frequency components is amplified. In other words, the seismic Hilbert energy shifts from the high-frequency components to the low-frequency components. Due to the aforementioned amplification and attenuation effects of the weak zone, the seismic Hilbert energy at the crest and the toe of the sliding mass is mainly in the frequency components of 1–2 and 3–5 Hz, and the seismic Hilbert energy at the middle part of the sliding mass is mainly in the frequency components of 1–2 Hz, as shown in Fig. 7. The peak Hilbert energy transmission ratios decrease gradually with increasing input amplitude, both in the frequency ranges of 1–2 and 3–5 Hz, as shown in Fig. 11.

3.4 Analysis of Dynamic Failure Mechanism

Dynamic failure mechanism governs the initiation and progression of the slope failure under earthquakes. A good understanding on the failure mechanism of the earthquake-induced landslide is helpful for hazard mitigation. Based on the above analysis, the weak zone has a significant impact on the seismic Hilbert energy distribution in the frequency domain. The shaking table test results show that:

1. The seismic Hilbert energy in the sliding mass is larger than that in the sliding bed.
2. The seismic Hilbert energy in the high-frequency components shifts to the low-frequency components when the seismic wave propagates through the weak zone.
3. The total seismic Hilbert energy at the toe of the sliding mass is the largest, followed by the crest of the sliding mass, with the total seismic energy in the middle part of the sliding mass being the smallest.
4. The total seismic Hilbert energy of the crest and the toe of the sliding mass is mainly in the frequency ranges of 1–2 and 3–5 Hz, while the seismic Hilbert energy of the middle part of the sliding mass is mainly in the frequency range of 1–2 Hz.
5. The peak Hilbert energy transmission ratios of the weak zone decrease gradually with increasing input amplitude.

In order to demonstrate the failure process of the earthquake-induced landslide, a numerical simulation using FLAC³D was conducted in this study and the shear strain increment in the weak zone is analysed. The slope
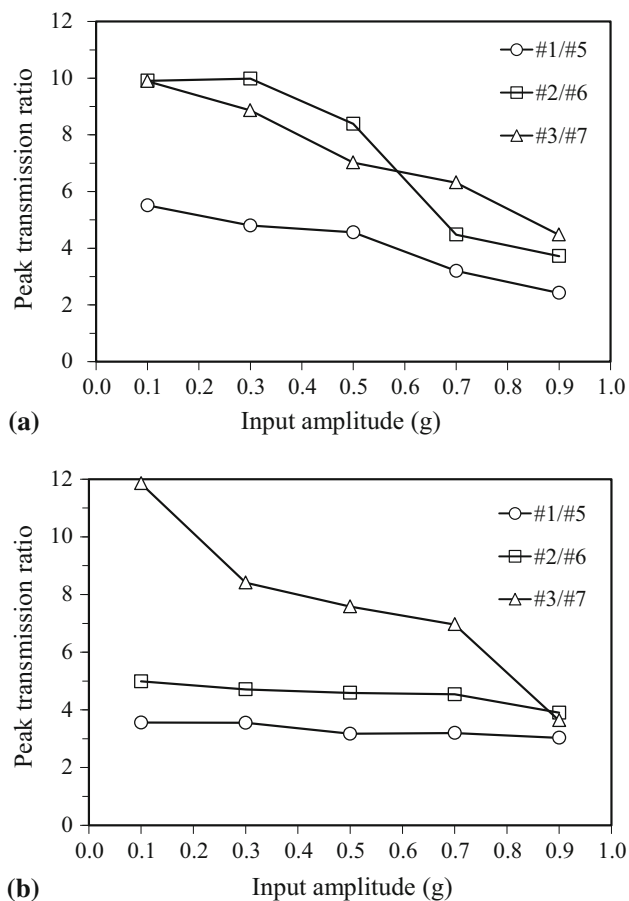
Fig. 11 Changes in the peak Hilbert energy transmission ratios with input seismic wave amplitude: **a** in the frequency range of 1–2 Hz and **b** in the frequency range of 3–5 Hz

geometry, material parameters, and input waveform for the FLAC^{3D} simulation model are all identical to those for the shaking table test model, as shown in Table 2. The Rayleigh damping with a minimum critical damping ratio of $\xi_{min} = 0.5\%$, a minimum central frequency of $\omega_{min} = 0.25$ Hz, and free boundary are assumed in the simulation model.

According to the results of the shaking table tests and the numerical simulations, the initiation and failure processes of the earthquake-induced landslide can be described as follows. When the input earthquake amplitude is 0.1 g, shear failure first develops at the crest and toe of the sliding mass, as shown in Fig. 12a. Larger and larger shear strain increments are observed in the weak zone under the excitations of 0.3, 0.5 and 0.7 g, but the zone with large shear strain increments does not extend throughout the whole weak zone, as shown in Fig. 12b, and no obvious dynamic failure was observed in the shaking table test model either. In these excitation stages, i.e. 0.3, 0.5 and 0.7 g, the marginal spectra peaks of #3 start to decrease. When the input amplitude reaches 0.9 g, large shear strain increments are observed in the whole weak zone, as shown

in Fig. 12c, and the marginal spectra peaks of #1 and #3 decrease dramatically as shown in Fig. 8, implying that the development of large shear strain increments in the weak zone dissipates much seismic Hilbert energy. Finally, a sliding surface forms, as shown in Fig. 13a, the slope loses its stability and the sliding mass slides with some tensile cracks at the trailing edge of the slope, as shown in Fig. 13b.

The initiation and progression of the landslide can be interpreted from the viewpoint of seismic Hilbert energy using the HHT and its marginal spectrum. In the process of seismic excitation, the seismic Hilbert energy stored in the sliding mass is larger than that in the sliding bed due to the superposition of the incident wave and the reflected wave near the slope surface. The seismic Hilbert energy difference between the sliding mass and the sliding bed will cause different dynamic responses between the sliding mass and the sliding bed, which may be an essential reason for the dynamic failures in the weak zone. When the seismic wave propagates through the weak zone, the high-frequency components are attenuated and the low-frequency components are amplified, causing the seismic Hilbert energy in the high-frequency components moving to the low-frequency components. Because of the influence of the weak zone on the seismic Hilbert energy distribution in the frequency domain, the seismic Hilbert energy of the crest and toe of the sliding mass is larger than that of the middle part. Much seismic Hilbert energy is carried in the frequency range of 3–5 Hz in the crest and toe of the sliding mass, as shown in Fig. 7. The aforementioned research shows that the natural frequency of the slope is 3.55 Hz. Hence, the seismic Hilbert energy in the frequency range of 3–5 Hz will intensify the dynamic response of the crest and the toe due to the resonance effect, and initiate the dynamic failures in the crest and toe of the sliding mass. Accordingly, the peaks of the marginal spectra in the frequency range of 3–5 Hz increase first and then decrease with increasing input amplitude, while the peaks of marginal spectra in the frequency range of 1–2 Hz increase with increasing input amplitude. In the process of shear failure in the weak zone, as more and more seismic Hilbert energy is dissipated in the weak zone with increasing input amplitude, the Hilbert energy transmission ratio of the weak zone decreases gradually, as shown in Fig. 11.

The differences in the acceleration time histories between the sliding bed and the sliding mass in the shaking table test are shown in Fig. 14, which implies an obvious dynamic response difference between the sliding mass and the sliding bed. Before the sliding surface forms, i.e. before the input amplitude is <0.9 g, the acceleration differences at the crest (#1–#5) and the toe (#2–#6) of the sliding mass are larger than that at the middle part (#3–#7) of the sliding
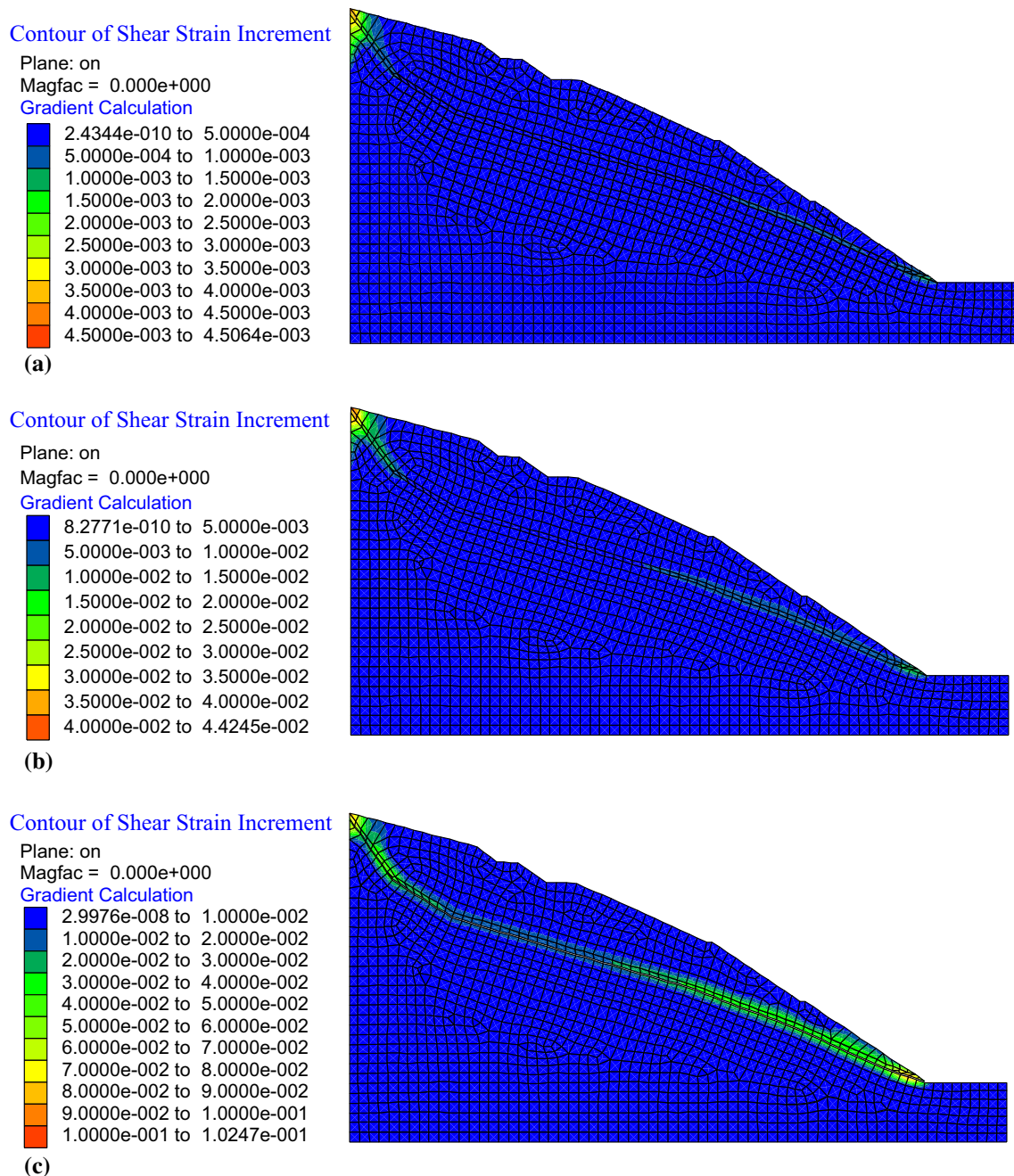
Fig. 12 Contours of shear strain increment in the weak zone under the seismic excitation of **a** 0.1 g, **b** 0.3 g and **c** 0.9 g El Centro earthquake waves

mass, indicating a nonuniform dynamic response in the sliding mass. In these excitation stages (0.1, 0.3, 0.5 and 0.7 g), the acceleration differences between the sliding mass and the sliding bed increase with increasing input amplitude. When the input amplitude reaches 0.9 g, a sliding surface forms, and the acceleration differences at the crest, the toe and the middle part of the sliding mass are similar, which implies that the dynamic response in the sliding mass becomes uniform after the formation of the sliding surface. The above analysis based on the measured

acceleration time histories in the shaking table tests supports the previous conclusion that the crest and toe of the sliding mass suffer stronger dynamic response differences than the middle part of the sliding mass in the initiation process of the earthquake-induced landslides.

The research in this paper shows three triggers for the earthquake-induced landslide: (1) the seismic Hilbert energy distribution difference between the sliding mass and the sliding bed, (2) the seismic Hilbert energy transition from high-frequency components to low-
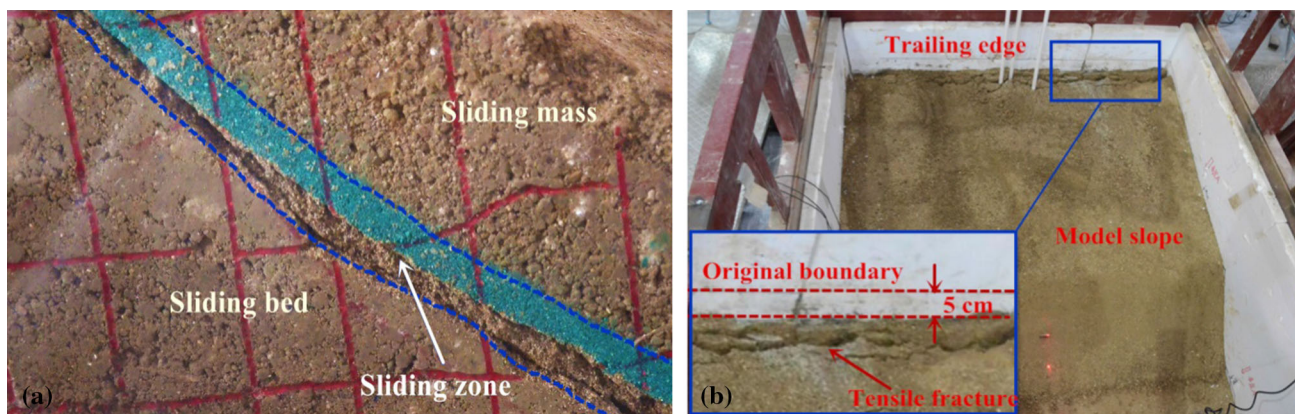
Fig. 13 Photographs showing **a** observed sliding surface and **b** tensile cracks at the trailing edge of the model slope in the shaking table test model after the seismic excitation of the 0.9 g El Centro earthquake wave
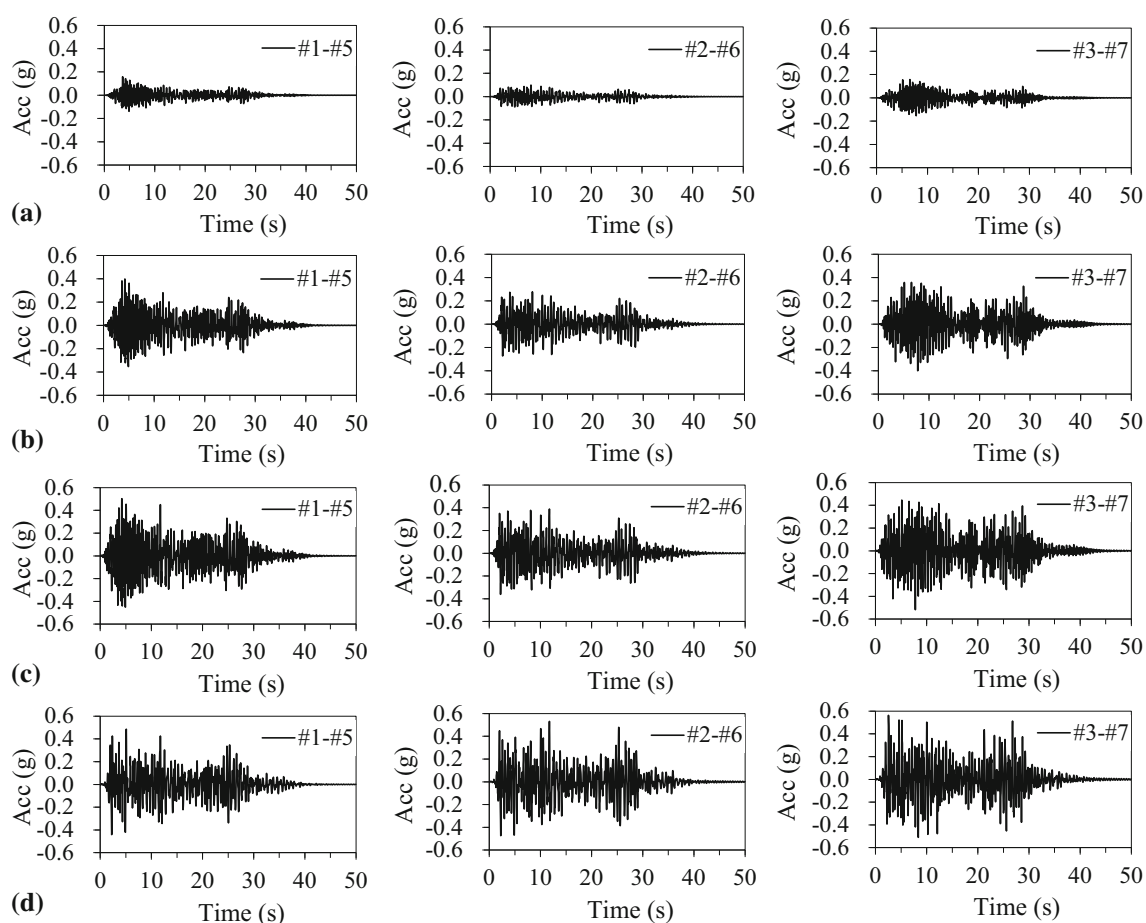

Fig. 14 Acceleration difference between the sliding mass and the sliding bed in the shaking table tests: **a** 0.1 g, **b** 0.3 g, **c** 0.5 g and **d** 0.9 g

frequency components and (3) the resonance effect at the crest and toe of the sliding mass. The dynamic failure first develops at the slope crest and the slope toe due to the resonance response and extends to the middle part of the weak zone. Finally a sliding surface forms, and the slope fails.

After the 12 May 2008 Wenchuan earthquake, Huang et al. (2011) pointed out that many landslides induced by the Wenchuan earthquake collapsed with the shattering-sliding failure type, including many large-scale and widely reported earthquake-induced landslides, such as the Daguangbao landslide, the Wangjiayan landslide and the

Donghekou landslide. The earthquake-induced landslide studied in this paper also falls in this failure type. Based on post-earthquake investigations and numerical simulations, cracks formed first at the slope crest and the lower part of the slope due to horizontal and vertical vibrations. Finally a sliding surface formed in the slope, and the slope shattered and slid. The proposed dynamic initiation and failure processes in this study coincide well with the field evidence reported by Huang et al. (2011).

4 Conclusions

An energy-based method for analysing mechanisms of earthquake-induced landslides is proposed based on Hilbert–Huang Transform (HHT) and its marginal spectrum, and a case study is presented in this paper. A large shaking table test was performed to illustrate the application of the proposed energy-based method to an earthquake-induced landslide with the shattering-sliding failure type. Then a FLAC^{3D} numerical model is developed to supplement the interpretation of the shaking table test. Based on this study, several conclusions can be drawn:

1. Since the HHT and its marginal spectrum represent the seismic Hilbert energy distribution in the frequency domain, it is feasible to identify changes of seismic Hilbert energy in the initiation and failure processes of an earthquake-induced landslide using the HHT and its marginal spectrum.
2. The seismic Hilbert energy in the sliding mass is larger than that in the sliding bed due to the superposition of the incident wave and the reflected wave near the slope surface, leading to different dynamic responses between the sliding mass and the sliding bed.
3. Because of the influence of the weak zone, the seismic Hilbert energy transfers from the high-frequency components to the low-frequency components.
4. At the slope crest and the slope toe, much seismic Hilbert energy is in the frequency range of 3–5 Hz, which is close to the natural frequency of the slope. Dynamic failure first develops at the slope crest and the slope toe due to the resonance response and then extends towards the middle part of the weak zone. Finally a sliding surface forms, and the slope fails.
5. Since more and more seismic Hilbert energy is dissipated in the weak zone during the formation of the slip zone, the peaks of the Hilbert energy transmission ratios decrease gradually with increasing input amplitude.
6. The proposed energy-based method has some limitations. As the seismic Hilbert energy distribution in the time domain is not considered in this method, determining the failure time of the slope is difficult. Charactering the initiation mechanism and failure process of the earthquake-induced landslide using seismic Hilbert energy required additional efforts.

Appendix

The EMD will reduce the data into a collection of IMFs defined as functions which satisfy the following conditions:

1. The number of extreme values and the number of zero-crossings must either equal or differ at most by one in the whole data set, and
2. The mean value of the envelope defined by the local maxima and the envelope defined by the local minima is zero at any point.

After the EMD, the original signal $a(t)$ is decomposed into n IMF components c_j and a residual r_n, which can either be the mean trend or a constant. The original data can be expressed as

$$a(t) = \sum_{j=1}^{n} c_j + r_n. \tag{1}$$

An EMD example of the original El Centro earthquake, which yields seven IMF components, is illustrated in Fig. 15.

Having obtained the IMF components, one will have no difficulty in applying the Hilbert transform to each IMF component, and computing the instantaneous frequency of each IMF component according to the Hilbert transform. For an arbitrary time series $X(t)$, its Hilbert transform $Y(t)$ can be defined as:

$$Y(t) = \frac{1}{\pi} P \int_{-\infty}^{\infty} \frac{X(t')}{t - t'} dt', \tag{2}$$

where P represents the Cauchy principal value, t represents time, with $X(t)$ and $Y(t)$ forming the complex conjugate pair. An analytical signal $Z(t)$ can be defined as:

Fig. 15 Original El Centro earthquake wave and EMD results
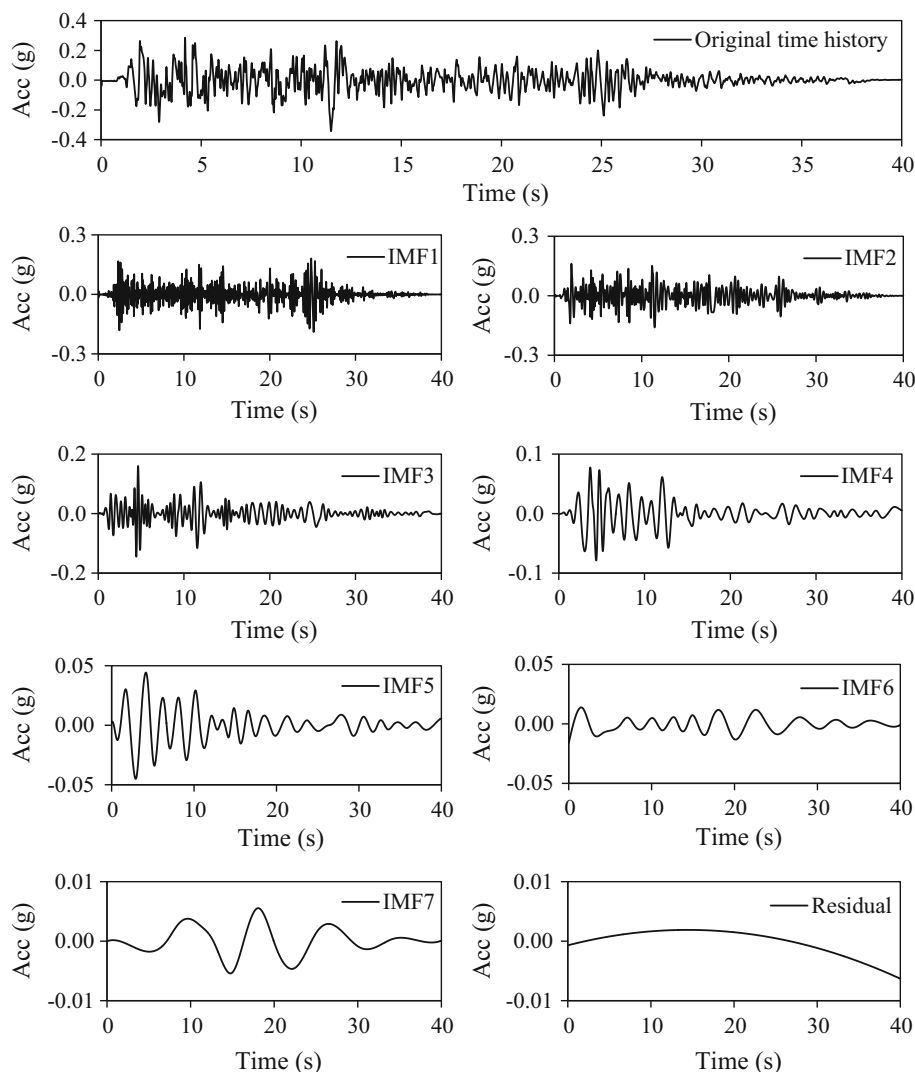
$$Z(t) = X(t) + iY(t) = a(t)e^{i\theta(t)}. \tag{3}$$

In which $a(t)$ and $\theta(t)$ are defined as:

$$a(t) = [X^2(t) + Y^2(t)]^{1/2}, \tag{4}$$

$$\theta(t) = \arctan[Y(t)/X(t)], \tag{5}$$

where $\theta(t)$ is the instantaneous phase, and the instantaneous frequency ω is defined as:

$$\omega = \frac{d\theta(t)}{dt}. \tag{6}$$

The instantaneous frequencies of the IMFs of the original El Centro earthquake wave are calculated and illustrated in Fig. 16. After performing the Hilbert transform on

each IMF component, the original data can be expressed as the real part, RP, in the following form:

$$X(t) = \mathrm{RP} \sum_{j=1}^{n} a_j(t) \exp\left[i \int \omega_j(t)dt\right]. \tag{7}$$

This frequency–time–amplitude distribution in Eq. (7) is designated as the Hilbert amplitude spectrum, $H(\omega, t)$, or simply the Hilbert spectrum. The Hilbert spectrum of the original El Centro earthquake wave is computed and shown in Fig. 17. The Hilbert spectrum, i.e. Eq. (7), shows that the Hilbert energy and instantaneous frequency of the original signal are functions of time t in a three-dimensional plot, in which the Hilbert energy can be contoured on the frequency–time plane.

Fig. 16 Instantaneous frequencies of the IMFs of the original El Centro earthquake wave
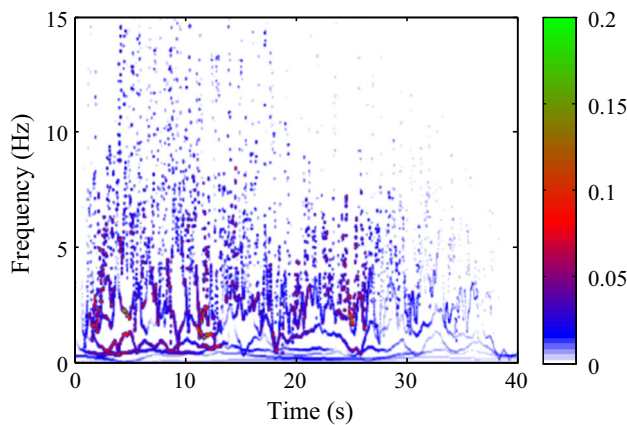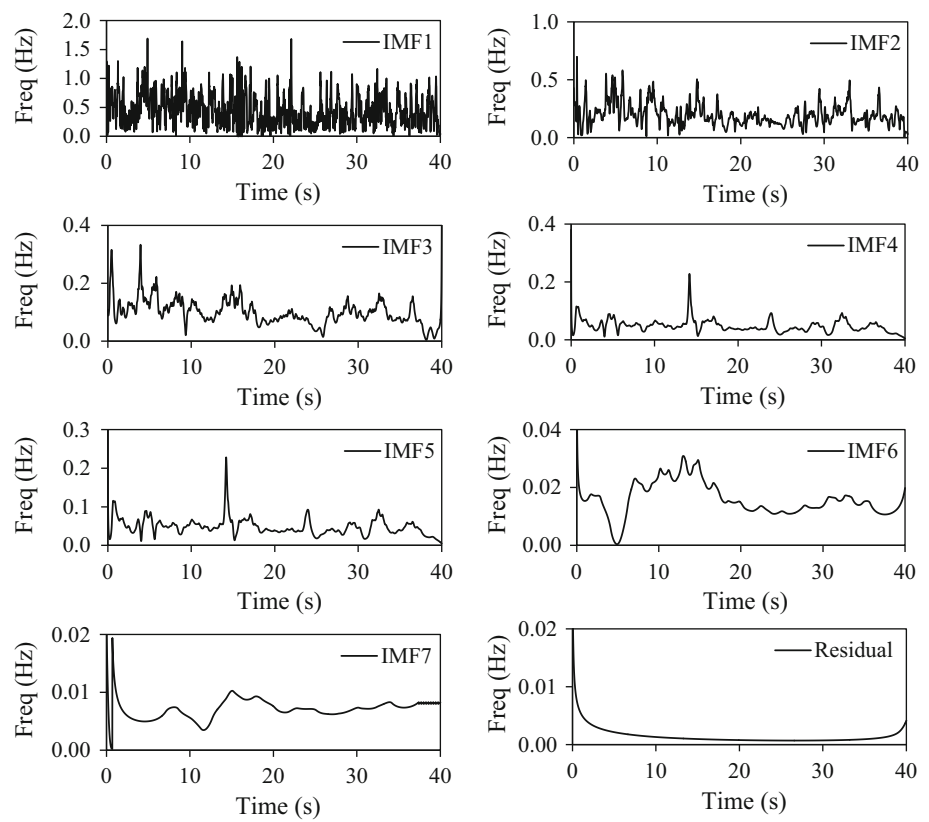

Fig. 17 Hilbert spectrum of the original El Centro earthquake wave

Fig. 18 Marginal spectrum of the original El Centro earthquake wave

With the Hilbert spectrum defined, the marginal spectrum, $h(\omega)$, can be defined as

$$h(\omega) = \int_0^T H(\omega, t) \mathrm{d}t. \tag{8}$$

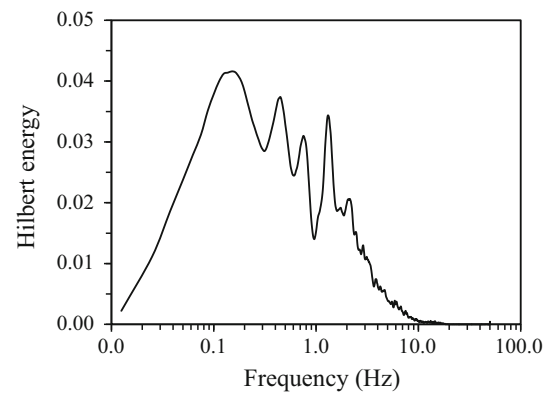The marginal spectrum of the original El Centro earthquake wave is shown in Fig. 18.

References

Ambraseys NN, Douglas J (2003) Near-field horizontal and vertical earthquake ground motions. Soil Dyn Earthq Eng 23:1–18

Bjerrum LW, Atakan K, Sørensen MB (2010) Reconnaissance report and preliminary ground motion simulation of the 12 May 2008 Wenchuan earthquake. Bull Earthq Eng 8:1569–1601

Bozorgnia Y, Niazi M, Campbell KW (1995) Characteristics of free-field vertical ground motion during the Northbridge earthquake. Earthq Spectra 17(4):515–525

Champati PK, Dimri S, Lakhera RC, Sati S (2007) Fuzzy-based method for landslide hazard assessment in active seismic zone of Himalaya. Landslides 4:101–111

Chang KJ, Taboada A, Lin ML, Chen RF (2005) Analysis of landsliding by earthquake shaking using a block-on-slope thermo-mechanical model: example of Jiufengershan landslide, central Taiwan. Eng Geol 80:151–163

Chen BR, Feng XT, Li QP, Luo RZ, Li SJ (2015) Rock burst intensity classification based on the radiated energy with damage intensity at Jinping II hydropower station, China. Rock Mech Rock Eng 48:289–303

Crockett RGM, Gillmore GK (2010) Spectral-decomposition techniques for the identification if radon anomalies temporally associated with earthquakes occurring in the UK in 2002 and 2008. Nat Hazards Earth Syst 10:1079–1084

Dai FC, Xu C, Yao X, Xu L, Tu XB, Gong QM (2011) Spatial distribution of landslides triggered by the 2008 Ms 8.0 Wenchuan earthquake, China. J Asian Earth Sci 40:883–895

Ding MT, Hu KH (2014) Susceptibility mapping of landslides in Beichuan County using cluster and MLC methods. Nat Hazards 70:755–766

Dong YF, Li YM, Xiao MK, Lai M (2008) Analysis of earthquake ground motions using an improved Hilbert–Huang transform. Soil Dyn Earthq Eng 28:7–19

Dong YF, Li YM, Lai M (2010) Structural damage detection using empirical-mode decomposition and vector autoregressive moving average model. Soil Dyn Earthq Eng 30:133–145

Fan G, Zhang JJ, Wu JB, Yan KM (2016a) Dynamic response and dynamic failure mode of a weak intercalated rock slope using a shaking table. Rock Mech Rock Eng 49:3243–3256

Fan G, Zhang JJ, Fu X (2016b) Transfer function analysis in shaking table test of site. Rock Soil Mech 37:2869–2876 **(in Chinese)**

Fan G, Zhang JJ, Fu X (2017) Research on transfer function of bedding rock slope with soft interlayer and its application. Rock Soil Mech. doi:10.16285/j.rsm.2017.04 **(in Chinese)**

Feng Z (2011) The seismic signatures of the 2009 Shiaolin landslide in Taiwan. Nat Hazards Earth Syst 11:1559–1569

Grelle G, Guadagno FM (2013) Regression analysis for seismic slope instability based on a double phase viscoplastic sliding model of the rigid block. Landslides 10:583–597

Grelle G, Revellino FM, Guadagno FM (2011) Methodology for seismic and post-seismic stability assessment of natural clay slopes based on a viscoplastic behaviour model in simplified dynamic analysis. Soil Dyn Earthq Eng 31:1248–1260

Guo D, Hamada M (2013) Qualitative and quantitative analysis on landslide influential factors during Wenchuan earthquake: a case study in Wenchuan County. Eng Geol 152:202–209

Hao TS, Liang WG (2016) A new improved failure criterion for salt rock based on energy method. Rock Mech Rock Eng 49:1721–1731

Huang RQ, Li WL (2009) Analysis of the geo-hazards triggered by the 12 May 2008 Wenchuan Earthquake, China. Bull Eng Geol Environ 68:363–371

Huang NE, Shen Z, Long SR, Wu MC, Shih HH, Zheng QA, Yen NC, Tung CC, Liu HH (1998) The empirical mode decomposition and Hilbert spectrum for nonlinear and non-stationary time series analysis. Proc R Soc A 454:903–995

Huang NE, Shen Z, Long SR (1999) A new view of nonlinear water waves: the Hilbert Spectrum. Annu Rev Fluid Mech 31:417–457

Huang NE, Wu ML, Qu WD, Long SR, Shen SS (2003) Applications of Hilbert–Huang transform to non-stationary financial time series analysis. Appl Stoch Model Bus Ind 19:245–268

Huang RQ, Xu Q, Huo JJ (2011) Mechanism and geo-mechanics models of landslides triggered by 5.12 Wenchuan earthquake. J Mt Sci 8:200–210

Huang RQ, Pei XJ, Fan XM, Zhang WF, Li SG, Li BL (2012) The characteristics and failure mechanism of the largest landslide triggered by the Wenchuan earthquake, May 12, 2008, China. Landslides 9:131–142

Ju JW (1989) On energy-based coupled elastoplastic damage theories: constitutive modeling and computational aspects. Int J Solids Struct 25:803–833

Li XP, He SM, Luo Y, Wu Y (2012) Simulation of the sliding process of Donghekou landslide triggered by the Wenchuan earthquake using a distinct element method. Environ Earth Sci 65:1049–1054

Liu HX, Xu Q, Li YR, Fan XM (2013) Response of high-strength rock slope to seismic waves in a shaking table test. Bull Seismol Soc Am 103:3012–3025

Liu HX, Xu Q, Li YR (2014) Effect of lithology and structure on seismic response of steep slope in a shaking table test. J Mt Sci 11(2):371–383

Meng QB, Zhang MW, Han LJ, Pu H, Nie TY (2016) Effects of acoustic emission and energy evolution of rock specimens under the uniaxial cyclic loading and unloading compression. Rock Mech Rock Eng 49:3873–3886

Munoz H, Taheri A, Chanda EK (2016) Fracture energy-based brittleness index development and brittleness quantification by pre-peak strength parameters in rock uniaxial compression. Rock Mech Rock Eng 49:4587–4606

Peng WF, Wang CL, Chen ST, Lee ST (2009) Incorporating the effects of topographic amplification and sliding areas in the modeling of earthquake-induced landslide hazards, using the cumulative displacement method. Comput Geosci 35:946–966

Peng RD, Ju Y, Wang JG, Xie HP, Gao F, Mao LT (2015) Energy dissipation and release during coal failure under conventional triaxial compression. Rock Mech Rock Eng 48:509–526

Poon CW, Chang CC (2007) Identification of nonlinear elastic structures using empirical mode decomposition and nonlinear normal modes. Smart Struct Syst 3(2):423–437

Rehman N, Mandic DP (2010) Multivariate empirical mode decomposition. Proc R Soc A 466:1291–1302

Tang CA, Kaiser PK (1998) Numerical simulation of cumulative damage and seismic energy release during brittle rock failure—part I: fundamentals. Int J Rock Mech Min 35:113–121

Tang CL, Hu JC, Lin ML, Angelier J, Lu CY, Chan YC, Chu HT (2009) The Tsaoling landslide triggered by the Chi-Chi earthquake, Taiwan: insights from a discrete element simulation. Eng Geol 106:1–19

Theodulidis NP, Bard PY (1995) Horizontal to vertical spectral ratio and geological conditions: an analysis of strong motion data from Greece and Taiwan (SMART-1). Soil Dyn Earthq Eng 14:177–197

Whitman R, Lambe P (1986) Effect of boundary conditions upon centrifuge experiments using ground motion simulation. Geotech Test J 9:61–71

Wu JH, Lin JS, Chen CS (2009) Dynamic discrete analysis of an earthquake-induced large-scale landslide. Int J Rock Mech Min 46(2):397–407

Yin YP, Wang FW, Sun P (2009) Landslide hazards triggered by the 2008 Wenchuan earthquake, Sichuan, China. Landslides 6:139–152

Yu CW, Chung JL, Wen YH, Huei TC (2010) Application of Hilbert–Huang transform to characterize soil liquefaction and quay wall seismic responses modeled in centrifuge shaking-table tests. Soil Dyn Earthq Eng 30:614–629

Zhang ZX, Kou SQ, Jiang LG, Lindqvist PA (2000) Effects of loading rate on rock failure: failure characteristics and energy partitioning. Int J Rock Mech Min 37:745–762

Zhang S, Zhang LM, Glade T (2014) Characteristics of earthquake- and rain-induced landslides near the epicenter of Wenchuan earthquake. Eng Geol 175:58–73

Zhang J, Peng WH, Liu FY, Zhang HX, Li ZJ (2016) Monitoring rock failure processes using the Hilbert–Huang Transform of acoustic emission signals. Rock Mech Rock Eng 49:427–442

Zhou JW, Cui P, Fang H (2013) Dynamic process analysis for the formation of Yangjiagou landslide-dammed lake triggered by the Wenchuan earthquake, China. Landslides 10:331–342